

1 Controls on the seafloor exposure of detachment fault surfaces

2
3
4 **Jean-Arthur Olive^{1*}, Ross Parnell-Turner^{2,3}, Javier Escartín⁴, Deborah K. Smith⁵, and**
5 **Sven Petersen⁶**

6
7 ¹*Laboratoire de Géologie, Ecole Normale Supérieure / CNRS UMR 8538, PSL Research*
8 *University, 24 rue Lhomond, 75005, Paris, France.*

9 ²*Woods Hole Oceanographic Institution, 266 Woods Hole Rd., Woods Hole MA, 02543, USA.*

10 ³*Now at: Scripps Institution of Oceanography, Institute of Geophysics and Planetary Physics,*
11 *University of California, San Diego, La Jolla, CA 92093, USA*

12 ⁴*Institut de Physique du Globe de Paris – CNRS UMR 7154, 1 rue Jussieu, 75005, Paris,*
13 *France.*

14 ⁵*National Science Foundation, 2415 Eisenhower Ave., Alexandria, VA, 22314, USA.*

15 ⁶*GEOMAR / Helmholtz Centre for Ocean Research, Wischhofstrasse 1-3, 24148, Kiel, Germany.*

16
17 *Corresponding author: olive@geologie.ens.fr

19 **Keywords**

20 Mid-ocean ridge; detachment faulting; oceanic core complex; critical taper; fault friction;

21

22 **Highlights**

23 • A small fraction of corrugated detachment fault surfaces is eventually exposed at the seafloor.
24 • Seafloor slopes indicate effective friction of ~0.2 on shallow part of detachments.
25 • Moderate-offset detachment faults may be largely blanketed by hanging wall material.
26 • Seafloor-shaping processes profoundly alter the morphology of oceanic core complexes.

27

28

29 **Abstract**

30 While oceanic detachment faults have been proposed to account for the accretion of ~40% of new
31 seafloor in the North Atlantic ocean, clear exposures of large-offset, often-corrugated fault
32 surfaces remain scarce and spatially limited. To help resolve this paradox, we examine the
33 conditions under which detachment fault growth may or may not lead to extensive exposure of
34 corrugated fault planes at the seafloor. Using high-resolution bathymetry from four detachment
35 faults at the northern Mid-Atlantic Ridge, we investigate the rafting of hanging wall-derived debris
36 over emerging fault scarps, which can lead to covering shallow-dipping corrugated fault surfaces.
37 We model this process using critical taper theory, and infer low effective friction coefficients
38 (~0.2) on the shallowest portion of detachment faults. A corollary to this result is that detachments
39 emerging from the seafloor at angles <13° are more likely to become blanketed under an apron of
40 hanging wall material. We generalize these findings as a simple model for the progressive exposure
41 and flexural rotation of detachment footwalls, which accounts for the continued action of seafloor-
42 shaping processes. Our model suggests that many moderate-offset, hidden detachment faults may
43 exist along slow mid-ocean ridges, and do not feature an exposed fault surface.

44

45 **1. Introduction**

46 Bathymetric highs composed of mafic and ultramafic units are a characteristic feature of slowly
47 accreted seafloor. These massifs are often capped by corrugated slip surfaces that represent the
48 rotated footwalls of detachment faults with offsets on par with or greater than the thickness of
49 young oceanic lithosphere (Cann et al., 1997; Tucholke et al., 1998; Parnell-Turner et al., 2018).
50 These faults are generally found on ridge sections characterized by greater-than-average seismicity
51 rates, lava geochemistry indicative of deeper fractionation, and hydrothermal activity (deMartin et
52 al., 2007; McCaig et al., 2007; Escartín et al., 2008b; Blackman et al., 2011; Wilson et al., 2013;
53 Olive and Escartín, 2016). Such observations led Escartín et al. (2008b) to postulate that
54 detachment faulting enables a distinct mode of asymmetric seafloor spreading, favored wherever
55 the magma supply of a mid-ocean ridge is subdued (Buck et al., 2005; Tucholke et al., 2008; Olive
56 et al., 2010).

57 Significant portions of seafloor in the North Atlantic ocean are presently forming through
58 asymmetric spreading (Escartín et al., 2008b; Cann et al., 2015). However, seafloor exposures
59 of corrugated fault surfaces, a telltale sign of detachment fault growth (Cann et al., 1997), are often

60 spatially confined (≤ 10 km along-axis; Fig. 1) and only make up a small fraction of the > 40 km-
61 long asymmetric sections of slow-spreading ridges. One explanation may be that detachment faults
62 underlie entire ridge segments but are only exposed in areas where hanging wall rider blocks
63 cannot develop (Smith et al., 2008; Reston and Ranero, 2011). Another is that detachment faults
64 have a limited along-axis extent and connect with shorter-offset faults through complex relay
65 structures (Smith et al., 2008; Tian and Choi, 2017). This debate warrants an improved
66 understanding of how various seafloor-shaping processes modulate the exposure of pristine slip
67 surfaces during detachment fault growth. These processes include gravitational mass wasting,
68 which can both erode and cover portions of the footwall (Cannat et al., 2013), as well as rafting of
69 hanging wall material onto the footwall. Here we investigate the mechanical and geometrical
70 factors that lead to covering an emerging detachment surface under a hanging wall apron, making
71 large-offset fault surfaces difficult to detect in shipboard bathymetric data. We then assess the
72 relative impact of hanging wall rafting and mass wasting on the shape of oceanic detachment faults.
73

74 **2. Seafloor morphology near oceanic detachment faults**

75 Fig. 1 shows high-resolution (< 2 m) bathymetry acquired using autonomous underwater vehicles
76 at four detachment faults along the Northern Mid-Atlantic Ridge: $13^{\circ}20'N$ (Escartín and Petersen,
77 2017; Escartín et al., 2017), $16^{\circ}36'N$ and South Core Complex (SCC; Smith et al., 2014), and the
78 Trans-Atlantic Geotraverse (TAG) detachment (Petersen et al., 2016). Geological interpretations
79 of bathymetric features and textures, combined with in-situ observations at $13^{\circ}20'N$, suggest a
80 common sequence of morphological domains at these detachments. The footwall cut-off scarp
81 (i.e., the breakaway high marking the initial location of fault emergence) is often texturally rough
82 (e.g., Fig. 1C), which is interpreted as the result of extensive gravitational mass wasting (Escartín
83 et al., 2017). Towards the ridge axis, this chaotic terrain gradually transitions into the corrugated
84 fault surface (Fig. 1A–D). This transition marks the place where angular blocks and talus stripped
85 from the breakaway ridge no longer blanket freshly exposed corrugated fault surfaces. This
86 difference is likely because the initially steep surface of growing detachments eventually rotates
87 to gravitationally stable angles ($< 30^{\circ}$, Lavier et al., 1999), which are no longer prone to mass
88 wasting (Cannat et al., 2013; Smith et al., 2014; Escartín et al., 2017).

89 The spatial extent of exposed corrugated surfaces varies greatly from one detachment to
90 another. At the $13^{\circ}20'N$ and SCC detachments, for example, the corrugated terrain exceeds 10 km^2

91 and abruptly connects with a rougher region termed "apron", axis-ward of the bathymetric moat
92 that marks the fault termination or hanging wall cut-off (break in slope in Fig. 2). At 13°20'N the
93 apron consists of basaltic and diabase blocks in an unlithified matrix, and incorporates some
94 footwall-derived peridotite and gabbro (Escartín et al., 2017). The apron surface has a texture that
95 is distinct from the adjacent volcanic terrain covering the ridge axis, and in many instances is thin
96 enough for the underlying corrugations to be visible beneath (Fig. 1A–D; Fig. 3A). At TAG, the
97 apron spans an area wider than the corrugated surface (Fig. 1A), and is directly adjacent to the
98 chaotic terrain south of 26°09'N. This geometry suggests that the apron has the potential to blanket
99 large extents of the detachment surface when certain geometrical and rheological conditions are
100 met.

101

102 **3. Detachment aprons as extensional Coulomb wedges**

103 To understand how hanging wall material may be dragged onto the emerging fault surface, we
104 model the apron as a cohesionless, critical Coulomb wedge of seafloor slope α with friction angle
105 ϕ_0 (30°, appropriate for mafic lithologies) overlying a detachment fault of dip β and friction angle
106 ϕ_D (Fig. 3A, Davis et al., 1983; Dahlen, 1984; Xiao et al., 1991; Yuan et al., 2015). We specifically
107 use the critical wedge model of Yuan et al. (2015), which accounts for the possibility of fluid
108 overpressure in the detachment. The fundamental assumption of wedge models is that the state of
109 stress in the apron results from a balance between topographic and frictional forces and is on the
110 verge of failure everywhere in critical wedges. The assumption of a cohesionless material is
111 consistent with observations of the 13°20'N detachment suggesting that the apron consists of a
112 mixture of unconsolidated rubble and finer-grained materials (Escartín et al., 2017).

113 We describe the state of stress within the wedge using two quantities ψ_D and ψ_0 , which
114 denote the angles between the most compressive principal stress (σ_1) and the detachment and apron
115 surface, respectively. These are useful to determine potential slip lines within the apron, which are
116 expected to lie at ($\pm 45^\circ - \phi_0/2$) from σ_1 (Fig. 3A). By definition, the critical taper angle for the apron
117 verifies:

$$118 \quad \alpha + \beta = \psi_D - \psi_0 . \quad (1)$$

119 If the entire apron is on the verge of Mohr-Coulomb failure, then only certain values of α , ψ_D and
120 ψ_0 are admissible for a given β . These values verify the following set of implicit equations:

121
$$\frac{\sin \alpha'}{\sin \phi_0} - \sin(2\psi_0 + \alpha') = 0 , \quad (2)$$

122 and

123
$$\sin(2\psi_D + \phi_D) - \frac{1 - \lambda_D}{1 - \lambda_0} \frac{\sin \phi_D}{\sin \phi_0} - \frac{\lambda_D - \lambda_0}{1 - \lambda_0} \sin \phi_D \cos 2\psi_0 = 0 . \quad (3)$$

124 In equation (2), α' is defined as an angle verifying

125
$$\tan \alpha' = \frac{1 - \rho_f / \rho}{1 - \lambda_0} \tan \alpha , \quad (4)$$

126 where λ_0 and λ_D denote the fluid pressure ratio in the apron and detachment, respectively. The fluid
127 pressure ratio is defined following Yuan et al. (2015) as

128
$$\lambda = -\frac{p_f - \rho_f g D}{\sigma_z + \rho_f g D} , \quad (5)$$

129 with

130
$$\sigma_z = -\rho g z \cos \alpha - \rho_f g D . \quad (6)$$

131 In equations (5) and (6), p_f is fluid pressure at a point located at a seafloor-normal distance z
132 beneath the apron surface (notation "D2" in Yuan et al., 2015). D is the water depth, and ρ and ρ_f
133 refer to the density of the apron material (2400 kg m^{-3}) and of the fluid percolating within the apron
134 (1000 kg m^{-3}). We assume that seawater easily percolates into the heavily damaged apron (Escartin
135 et al., 2017), and exerts a hydrostatic fluid pressure throughout the wedge, i.e., fluid pressure
136 increases downward in the wedge following a hydrostatic gradient. It can be shown that equation
137 (5) reduces to $\lambda = \rho_f / \rho$ under hydrostatic conditions (see Appendix A. of Yuan et al. 2015). The
138 fluid pressure ratio is thus set equal to 0.42 within the apron for the remainder of our study.

139 Equations (1-3) are formulated in terms of a residual function $F(\alpha, \psi_D, \psi_0) = 0$, and solved
140 with a Newton method for a range of β -values. The associated Jacobian ∇F is estimated using
141 centered finite difference with a step of 10^{-6} rad. Convergence is considered achieved when the
142 norm of the residual falls below 10^{-11} . Our initial guess is $\alpha = \phi_0 / 2$, $\psi_0 = 20^\circ$, and ψ_D set to either
143 20° or 120° , which are empirically found to promote convergence towards the upper or lower
144 branch of the envelope, respectively. For a given pair of fault friction and fault fluid pressure
145 values, the slope of the apron and the dip of the detachment must satisfy a set of equilibrium
146 relations, plotted as stability envelopes in Fig. 3B. A MATLAB[®] script *GetWedgeEnvelope.m* is
147 provided as part of the Supplementary Materials to generate stability envelopes (combinations of

148 α and β) as a function of ϕ_0 , ϕ_D , λ_0 , and λ_D . This function calls the subroutines *wedge_residual.m*
149 (Residual function) and *wedge_jacobianFD.m* (Jacobian approximation), which are also provided.

150 Estimates for apron slope and detachment fault dip were obtained along 89 profiles oriented
151 parallel to the spreading direction, crossing the hanging-wall cutoff (or moat; see Fig. 2 and
152 3A). High-resolution bathymetry was extracted along profiles spaced 100 m apart at the four study
153 locations (Fig. 1). The position of the hanging-wall cutoff and spatial extent of the moat was
154 identified in map-view, based upon the locus of change in bathymetric slope, and then used to
155 define the hanging wall, footwall, and moat sections along each profile (Fig. 2). The mean apron
156 slope was estimated for each profile using the slope of a linear least-squares fit to the bathymetry
157 calculated over a 500 m distance downslope from the hanging wall-side edge of the moat, hence
158 the moat itself is not included in the fit. The mean detachment fault dip was estimated using the
159 slope of a linear fit to the bathymetry calculated 800 m upslope from the footwall-side edge of the
160 moat. Uniform fitting lengths were chosen for consistency and to minimize the effects of local
161 changes in slope, while not allowing profiles to extend onto the chaotic or neovolcanic terrains.
162 The average apron slope across our detachments is $6.2 \pm 3.3^\circ$ (1 standard deviation), and the average
163 detachment dip right beneath the hanging wall cutoff is $13.8 \pm 2.5^\circ$.

164

165 **4. Low effective friction on the shallow part of oceanic detachment faults**

166

167 We follow a grid search approach to identify the product $\mu_D (1-\lambda_D) = \tan(\phi_D)(1-\lambda_D)$ that best
168 explains the observed pair of $(\alpha, \beta > -\alpha)$ along 89 corrugation-parallel bathymetric transects at the
169 four detachments shown in Figs. 1 and 2. For each pair (α, β) , we construct 100 envelopes spanning
170 values of $0.42 \leq \lambda_D \leq 0.82$ and $0 \leq \phi_D \leq 30^\circ$. Each point on these envelopes corresponds to a specific
171 stress orientation, which determines the orientation of possible slip lines (secondary faults) within
172 the apron (Fig. 3A). We restrict our analysis to the upper branch of the envelopes, which predicts
173 net extension in the wedge. We retain the envelopes whose upper branch lies at the shortest
174 distance to each (α, β) pair, within an error of 2° (Fig. 3B). This set of best-fitting envelopes
175 correspond to a narrow subset of (λ_D, ϕ_D) space, and consequently to a narrow range of $\mu_D (1-\lambda_D)$
176 values. We repeat this operation for an entire grid of (α, β) values, to which we are able to assign
177 a best fitting $\mu_D (1-\lambda_D)$ with a typical error of ± 0.01 , plotted in Fig. 4 and as colored dots for each

profile in Fig. 1. For convenience, we also provide a polynomial approximation for $\mu_D(1-\lambda_D)$ as a function of (α, β) , in degrees, which is accurate within the above error margin:

$$\begin{aligned} \mu_D(1-\lambda_D) = & 0.008252 + 0.004973\beta - 0.003603\alpha + 0.00012\beta^2 + 1.026 \times 10^{-5}\alpha\beta + \\ & 7.116 \times 10^{-5}\alpha^2 - 1.853 \times 10^{-6}\beta^3 + 3.793 \times 10^{-7}\beta^2\alpha - 3.959 \times 10^{-6}\beta\alpha^2 - 2.385 \times \\ & 10^{-6}\alpha^3. \end{aligned} \quad (7)$$

The inversion procedure described above yields a range of $\mu_D(1-\lambda_D)$ between 0.06 and 0.16, with a mode at 0.14 (Fig. 4). Since the geometry of the detachment surface is concave-down, measuring fault dip at the termination may underestimate the true dip of the detachment beneath the apron region (Fig. 3A). Estimates of the sub-seafloor fault geometry (available only for TAG and 13°20'N: deMartin et al., 2007; Parnell-Turner et al., 2017) suggest that detachments may steepen by at most $\sim 10^\circ$ across the apron (see section 5). Underestimating the average detachment dip beneath the apron by $\sim 5^\circ$ would lead to underestimating $\mu_D(1-\lambda_D)$ by ~ 0.04 . Fig. 4 provides a straightforward way to assess the effect of an underestimated detachment dip (e.g., by translating the points towards the right by $\sim 5^\circ$).

Profiles located away from the center of detachments tend to yield lower values of $\mu_D(1-\lambda_D)$ (Fig. 1), which may be due to the termination strike being highly oblique to the spreading direction at these locations owing to the three-dimensional fault morphology. By contrast, profiles oriented normal to the termination (i.e., most compatible with the two dimensional nature of the critical wedge model and often located in the central part of the detachment) commonly yield $\mu_D(1-\lambda_D)$ values ranging between 0.10 and 0.16, which we consider to be more reliable. Some short-wavelength apparent variability in our estimates directly reflects second-order tectonic features that offset the fault termination and alter slopes (e.g., at SCC, N and S of 16.425°N, Fig. 1B). Our 2-D analysis is therefore unlikely to resolve frictional heterogeneities on a given detachment, if present.

Our estimates of $\mu_D(1-\lambda_D)$ can be translated into values of effective detachment friction, as defined by Dahlen (1984):

$$\mu_{eff} = \mu_D \frac{(1-\lambda_D)}{(1-\lambda_0)}. \quad (8)$$

This definition accounts for the buoyancy of fluids that percolate in the wedge. Under our assumption of hydrostatic fluid pressure in the apron ($\lambda_0 = 0.42$), we estimate effective friction coefficients between 0.17 and 0.28 in oceanic detachment faults. Low values of effective friction

208 are consistent with the common inference that the low strength of detachments enables their
209 longevity (Escartín et al., 1997). Our strength estimates are however only representative of the
210 uppermost ~1 km portion of detachments, which may be different from the rest of the fault. A
211 possible manifestation of this difference could be the lack of shallow (≤ 3 km) microseismicity
212 beneath TAG (deMartin et al., 2007) and 13°20'N (Parnell-Turner et al., 2017), as recorded by
213 local ocean bottom seismometers (OBS) arrays. While very low effective friction on
214 compressional décollements is typically attributed to elevated fluid pressure (e.g., Dahlen, 1984),
215 such a scenario may be harder to envision in a tensional regime where cracks and pores are likely
216 well connected. If fluid pressure is hydrostatic within the detachment fault zone, as was inferred
217 by Hansen et al. 2013 for the Kane detachment down to depths of ~5 km, then the true friction
218 coefficient of the fault material (μ_D) must lie between ~0.17 and ~0.26 (Fig. 3A). The precipitation
219 of very weak minerals such as talc, with friction coefficients ranging between ~0.05 and 0.23
220 (Moore and Lockner, 2008; Escartín et al., 2008a) in the fault zone has been invoked as a key
221 contributor to long-term strain localization (Escartín et al., 1997). By contrast, invoking
222 moderately weak clay minerals (with friction coefficients of ~0.4, e.g., Tesei et al., 2012) to explain
223 our estimates of effective friction would however require super-hydrostatic fluid pressure ratios
224 between 0.6 and 0.75. The 13°20'N detachment, however, does not feature extensive weak phases
225 (e.g., serpentinite, talc) and instead shows pervasive silicification (Bonnemains et al., 2017). The
226 low effective friction of detachments may instead have a non-lithological origin. Episodes of
227 seismic slip have been documented in the shallow, microseismically quiet portion of the 13°20'N
228 detachment (Craig and Parnell-Turner, 2017). It is possible that infrequent earthquakes
229 catastrophically reshape apron slopes to balance the low shear stresses that prevail during seismic
230 rupture. The temporally-averaged apron slopes we measure may thus be influenced both by the
231 long-term and the short-term fault strength, although this hypothesis is difficult to evaluate with
232 the available data.

233 The above reasoning relies on the assumption that the apron wedge is critically stable, i.e.,
234 sits on the stability envelope as shown in Fig. 3B. At the 13°20'N detachment, small escarpments
235 are visible in apron topography, potentially indicating secondary faulting (Fig. 3A). Internal wedge
236 deformation alone would be indicative of the unstable wedge regime (outside of the stability
237 envelope, Xiao et al., 1991). When coincident with slip on the detachment, secondary faulting
238 implies a critically-stable apron at 13°20'N. However, slip on other detachments may occur without

239 faulting in the apron. Such systems would plot inside the stability envelope. Since increasing
240 detachment friction shifts the stability boundary towards greater detachment dips (Hayman et al.
241 2003), one can identify the greatest value of detachment friction that allows a wedge of a given (α ,
242 β) to remain inside the stability envelope. This value corresponds to the critically-stable
243 configuration. In other words, the effective friction determined with our approach must be thought
244 of as an upper-bound on detachment strength.

245

246 **5. Implications for the seafloor exposure of detachment fault surfaces**

247 Regardless of the mechanistic interpretation for μ_{eff} , Coulomb wedge theory does predict
248 an effective value for detachment friction that explains apron architecture (including the pattern of
249 secondary faulting: Fig. 3A). A corollary to this model is that a detached piece of apron would not
250 remain affixed to the footwall if the fault emerges from the seafloor with a slope greater than
251 $\text{atan}(\mu_D(1 - \lambda_D)/(1 - \lambda_0)) \sim 13 \pm 3^\circ$ for $\mu_{eff} = 0.23 \pm 0.05$, because the low basal shear stresses would
252 not be able to counteract gravity. Pieces of apron would thus slide back towards the hanging wall
253 instead of blanketing the footwall. Conversely, a detachment fault emerging from the seafloor with
254 a slope $< 13^\circ$ should be extensively covered by hanging wall material.

255 The primary challenge in testing this idea is to infer detachment fault dip where it is not
256 exposed. Such estimates are possible at TAG and 13°20'N, which constitute low and high end-
257 members for the extent of the corrugated fault surface, respectively, and have both been
258 instrumented with OBS arrays to illuminate the deeper portions of the fault zone through
259 microseismicity (deMartin et al., 2007; Parnell-Turner et al., 2017). The clouds of extensional
260 microseismicity observed at the roots of TAG and 13°20'N show dips as large as 70° at depths of
261 ~ 7 km below seafloor. This clearly indicates an overall concave-down geometry of the detachment
262 at depth. High-resolution seismic imaging studies will be needed to improve our knowledge of the
263 near-surface geometry of these detachments. In the meantime, seafloor slopes reveal that a large
264 portion of the apron domain at TAG is underlain by a detachment dipping with angles $\leq 10^\circ$ (Fig.
265 2A), which is not the case at 13°20'N, where the fault emerges with slopes in excess of 15° (Fig.
266 2D). This simple comparison supports the idea that a gently dipping detachment is prone to
267 extensive blanketing by apron material, and less likely to feature extensive, well exposed
268 corrugated surfaces.

269

270 **6. From covered to exposed detachment surfaces**

271 Seafloor shaping processes are strongly sensitive to slope. Gravitational mass wasting is favored
272 along slopes with an angle of repose steeper than $\sim 20\text{--}30^\circ$ (Cannat et al., 2013). By contrast,
273 blanketing of exposed fault surfaces by hanging wall material is favored for shallow slopes $<13^\circ$.
274 The emerging slope of a detachment fault is known to change as the footwall undergoes flexural
275 re-adjustment with continued slip (Buck, 1988; Lavier et al., 1999; Morris et al., 2009). Fig. 5
276 illustrates this process using an elastic model for footwall topography with increasing fault offset
277 (Buck, 1988; Schouten et al., 2010; Olive and Behn, 2014). In the early stages of detachment
278 growth, a breakaway ridge forms by slip along a high angle ($>30^\circ$) fault, which triggers the
279 extensive mass wasting that shapes the chaotic terrain (Fig. 5A). The morphology of young
280 detachments may thus be strongly determined by the competition between the rate of footwall
281 degradation by repeated rockslides, and the fault slip rate. Hence, efficient mass wasting could
282 very well bury short-offset corrugated surfaces under footwall-derived debris.

283 As fault offset increases, flexural rotation decreases the emerging detachment slope until
284 it becomes sub-horizontal (Fig. 5B). This stage favors extensive blanketing of the corrugated fault
285 surface by hanging wall material, as seen today at TAG, a detachment fault with only ~ 5 km of
286 offset (deMartin et al., 2007). Further extension on the detachment drives footwall doming (Fig.
287 5C), which increases the slope of the emerging footwall ($>13^\circ$) and shrinks the apron domain,
288 revealing an extensive corrugated surface (e.g., $13^\circ 20' \text{N}$, with 9 km of offset). It should be noted
289 that the emergence angle will to some extent also reflect the amount of volcanic material extruded
290 onto the hanging wall (magmatic accretion in Fig. 5A).

291 Our model suggests that moderate-offset detachment faults may be widespread along slow-
292 spreading ridges but remain undetected by shipboard bathymetric surveys, as they are largely
293 blanketed by hanging wall material and do not (yet) expose large corrugated surfaces at the
294 seafloor. Extensive high-resolution bathymetric surveys and a better mechanistic description of
295 seafloor-shaping processes thus constitute crucial next steps to improve our understanding of slow-
296 spreading ridge tectonics.

297

298 **Acknowledgements**

299 The authors wish to thank the ODEMAR (doi:[10.17600/13030070](https://doi.org/10.17600/13030070)) and M127 Science Parties as
300 well as the teams operating the AUVs (WHOI's *Sentry* and GEOMAR's *Abyss*). JAO was funded

301 under NSF project EAR16500166. Cruise funding was provided through CNRS and IFREMER
302 (JE), and GEOMAR and the EU-FP7-Project “Blue Mining: Breakthrough Solutions for the
303 Sustainable Exploration and Extraction of Deep Sea Mineral Resources” under grant No. 604500
304 (SP). Xiaoping Yuan provided valuable guidance on the Coulomb wedge modeling. Finally, we
305 thank Nadaya Cubas, Nicholas Hayman, and an anonymous reviewer for their thoughtful
306 suggestions, which greatly improved our manuscript.

307

308 **References**

309 Blackman, D.K., et al., 2011, Drilling constraints on lithospheric accretion and evolution at
310 Atlantis Massif, Mid-Atlantic Ridge 30°N: *J. Geophys. Res.*, v. 116, no. B07103,
311 doi:10.1029/2010JB007931.

312 Bonnemains, D., Escartín, J., Mével, C., Andreani, M., and Verlaguet, A., 2017, Pervasive
313 silicification and hanging wall overplating along the 13°20'N oceanic detachment fault (Mid-
314 Atlantic Ridge): *Geochem. Geophys. Geosyst.*, v. 18, no. 6, p. 2028–2053,
315 doi:10.1002/2017GC006846.

316 Buck, W.R., 1988, Flexural Rotation of Normal Faults: *Tectonics*, v. 7, no. 5, p. 959–973, doi:
317 10.1029/TC007i005p00959.

318 Buck, W.R., Lavier, L., and Poliakov, A.N.B., 2005, Modes of faulting at mid-ocean ridges:
319 *Nature*, v. 434, p. 719–723, doi: 10.1038/nature03358.

320 Cann, J.R., Blackman, D.K., Smith, D.K., McAllister, E., Janssen, B., Mello, S., Avgerinos, E.,
321 Pascoe, A.R., and Escartín, J., 1997, Corrugated slip surfaces formed at North Atlantic ridge-
322 transform intersections: *Nature*, v. 385, p. 329–332.

323 Cann, J.R., Smith, D.K., Escartín, J., and Schouten, H., 2015, Tectonic evolution of 200 km of
324 Mid-Atlantic Ridge over 10 million years — Interplay of volcanism and faulting: *Geochem.*
325 *Geophys. Geosyst.*, v. 16, p. 2303–2321, doi:10.1002/2015GC005797.

326 Cannat, M., Mangeney, A., Ondréas, H., Fouquet, Y., and Normand, A., 2013, High-resolution

327 bathymetry reveals contrasting landslide activity shaping the walls of the Mid-Atlantic Ridge
328 axial valley: *Geochem., Geophys., Geosyst.*, v. 14, no. 4, p. 996–1011,
329 <http://doi.org/10.1002/ggge.20056>.

330

331 Craig, T.J., Parnell-Turner, R., 2017. Depth-varying seismogenesis on an oceanic detachment fault
332 at 13°20'N on the Mid-Atlantic Ridge. *Earth Planet. Sci. Lett.*, v. 479, p. 60–70,
333 doi:10.1016/j.epsl.2017.09.020.

334

335 Collins, J.A., Smith, D.K., and McGuire, J.J., 2012. Seismicity of the Atlantis Massif detachment
336 fault, 30°N at the Mid-Atlantic Ridge: *Geochem. Geophys. Geosyst.*, v. 13, no. 1, p.
337 doi:10.1029/2012GC004210, doi: 10.1029/2012GC004210.

338 Dahlen, F.A., 1984, Noncohesive critical Coulomb wedges: An exact solution: *J. Geophys. Res.*,
339 v. 89, no. B12, p. 10,215–10,033.

340 Davis, D., Suppe, J., and Dahlen, F.A., 1983, Mechanics of fold-and-thrust belts and accretionary
341 wedges: *J. Geophys. Res.*, v. 88, no. B2, p. 1153–1172.

342 deMartin, B. J., Sohn, R.A., Canales, J.P., and Humphris, S.E., 2007, Kinematics and geometry of
343 active detachment faulting beneath the Trans-Atlantic Geotraverse (TAG) hydrothermal field
344 on the Mid-Atlantic Ridge: *Geology*, v. 35, p. 711–714, doi: 10.1130/G23718A.1.

345 Escartín, J., Hirth, G., and Evans, B., 1997, Effects of serpentinization on the lithospheric strength
346 and the style of normal faulting at slow-spreading ridges: *Earth Planet. Sci. Lett.*, v. 151, no.
347 3–4, p. 181–189, doi:10.1016/S0012-821X(97)81847-X.

348

349 Escartín, J., Andreani, M., Hirth, G., and Evans, B., 2008a, Relationships between the
350 microstructural evolution and the rheology of talc at elevated pressures and temperatures: *Earth*
351 *Planet. Sci. Lett.*, v. 268, p. 463–475.

352

353 Escartín, J., Smith, D.K., Cann, J.R., Schouten, H., Langmuir, C.H., and Escrig, S., 2008b, Central
354 role of detachment faults in accretion of slow-spreading oceanic lithosphere: *Nature*, v. 455,

355 no. 7214, p. 790–794, doi: 10.1038/nature07333.

356 Escartín, J., and Petersen, S., 2017, ODEMAR AUV Abyss (GEOMAR) + shipboard Pourquoi
357 Pas? Multibeam bathymetry – 13°20'N and 13°30'N Oceanic Core Complexes, Mid-Atlantic
358 Ridge: SEANOE, <http://doi.org/10.17882/48335>.

359 Escartín, J., Petersen, S., Bonnemains, D., Cannat, M., Andreani, M., Bezos, A., Chavagnac, V.,
360 Choi, Y., Godard, M., Haaga, K., Hamelin, C., Ildefonse, B., Jamieson, J., John, B., et al.,
361 2017, Tectonic structure, evolution, and the nature of oceanic core complexes and their
362 detachment fault zones (13°20' N and 13°30'N, Mid Atlantic Ridge): *Geochem. Geophys.*
363 *Geosyst.*, 18, doi:10.1002/2016GC006775.

364 Hansen, L.N., Cheadle, M.J., John, B.E., Swapp, S.M., Dick, H.J.B., Tucholke, B.E., and Tivey,
365 M.A., 2013, Mylonitic deformation at the Kane oceanic core complex: Implications for the
366 rheological behavior of oceanic detachment faults: *Geochem. Geophys. Geosyst.*, 14,
367 doi:10.1002/ggge.20184.

368 Hayman, N.W., Knott, J.R., Cowan, D.S., Nemser, E., and Sarna-Wojnicki, A.M., 2003,
369 Quaternary low-angle slip on detachment faults in Death Valley, California: *Geology*, v. 31,
370 no. 4, p. 343–346.

371 Lavier, L., Buck, W.R., and Poliakov, A., 1999, Self-consistent rolling-hinge model for the
372 evolution of large-onset low-angle normal faults: *Geology*, v. 27, no. 12, p. 1127–1130, doi:
373 10.1130/0091-7613(1999)027<1127:SCRHMF>2.3.CO;2.

374 McCaig, A.M., Cliff, R.A., Escartín, J., Fallick, A.E., and MacLeod, C.J., 2007, Oceanic
375 detachment faults focus very large volumes of black smoker fluids: *Geology*, v. 35, no. 10., p.
376 935–938.

377 Moore, D.E., and Lockner, D.A., 2008, Talc friction in the temperature range 25°–400°C:
378 Relevance for fault-zone weakening: *Tectonophysics*, v. 449, p. 120–132,
379 doi:10.1016/j.tecto.2007.11.039.

380 Morris, A., Gee, J.S., Pressling, N., John, B.E., MacLeod, C.J., Grimes, C.B., and Searle, R.C.,

381 2009, Footwall rotation in an oceanic core complex quantified using reoriented Integrated
382 Ocean Drilling Program core samples: *Earth Planet. Sci. Lett.*, v. 287, no. 1–2, p. 217–228,
383 doi: 10.1016/j.epsl.2009.08.007.

384 Olive, J.-A., Behn, M.D., and Tucholke, B.E., 2010, The structure of oceanic core complexes
385 controlled by the depth-distribution of magma emplacement: *Nat. Geosci.*, v. 3., p. 491–495,
386 doi:10.1038/ngeo888.

387 Olive, J.-A., and Behn, M.D., 2014, Rapid rotation of normal faults due to flexural stresses: An
388 explanation for the global distribution of normal fault dips: *J. Geophys. Res.*, 119,
389 doi:10.1002/2013JB010512.

390

391 Olive, J.-A., and Escartín, J., 2016, Dependence of seismic coupling on normal fault style along
392 the Northern Mid-Atlantic Ridge: *Geochem. Geophys. Geosyst.*, 17, 4128–4152, doi:10.1002/
393 2016GC006460

394

395 Parnell-Turner, R., Escartín, J., Olive, J.A., Smith, D.K., Petersen, S., 2018. Genesis of corrugated
396 fault surfaces by strain localization recorded at oceanic detachments. *Earth Planet. Sci. Lett.*
397 498, 116–128. doi:10.1016/j.epsl.2018.06.034

398

399 Parnell-Turner, R., Sohn., R.A., Peirce, C., Reston, T.J., MacLeod, C.J., Searle, R.C., and Simão,
400 N.M., 2017, Oceanic detachment faults generate compression in extension: *Geology*,
401 doi:10.1130/G39232.1.

402

403 Petersen, S., and Shipboard Scientific Party, 2016, Cruise report M127 –Metal fluxes and Resource
404 Potential at the Slow-spreading TAG Mid-ocean Ridge Segment (26°N, MAR)– Blue
405 Mining@Sea: GEOMAR report 32, doi: 10.3289/GEOMAR_REP_NS_32_2016.

406

407 Reston, T.J., and Ranero C.R., 2011, The 3-D geometry of detachment faulting at mid-ocean
408 ridges: *Geochem. Geophys., Geosyst.*, v. 12, no. 7, doi:10.1029/2011GC003666.

409

410 Schouten, H., Smith, D.K., Cann, J.R., and Escartin, J., 2010, Tectonic versus magmatic extension
411 in the presence of core complexes at slow-spreading ridges from a visualization of faulted
412 seafloor topography: *Geology*, v. 38, no. 7, p. 615–618, doi: 10.1130/G30803.1.

413 Smith, D.K., Escartin, J., Schouten, H., and Cann, J.R., 2008, Fault rotation and core complex
414 formation: Significant processes in seafloor formation at slow-spreading mid-ocean ridges
415 (Mid-Atlantic Ridge, 13°–15°N): *Geochem. Geophys. Geosyst.*, v. 9, no. 3, p.
416 doi:10.1029/2007GC001699, doi: 10.1029/2007GC001699.

417 Smith, D.K., Schouten, H., Dick, H.J.B., Cann, J.R., Salters, V., Marschall, H.R., Ji, F., Yoerger,
418 D., Sanfilippo, A., Parnell-Turner, R., Palmiotto, C., Zhelezov, A., Bai, H., Junkin, W., et al.,
419 2014, Development and evolution of detachment faulting along 50 km of the Mid-Atlantic
420 Ridge near 16.5°N: *Geochem. Geophys. Geosyst.*, v. 15, p. 4692–4711,
421 doi:10.1002/2014GC005563.

422 Spencer, J.E., Reynolds, S.J., Scott, R.J., and Richard, S.M., 2016, Shortening in the upper plate
423 of the Buckskin-Rawhide extensional detachment fault, southwestern U.S., and implications
424 for stress conditions during extension: *Tectonics*, v. 35, no. 12, p. 3119–3136,
425 doi:10.1002/2016TC004345.

426 Tesei, T., Collettini, C., Carpenter, B.M., Viti, C., and Marone, C., 2012, Frictional strength and
427 healing behavior of phyllosilicate-rich faults: *J. Geophys. Res.*, v. 117,
428 doi:10.1029/2012JB009204.

429 Tian, X., and Choi, E., 2017, Effects of axially variable diking rates on faulting at slow spreading
430 mid-ocean ridges: *Earth Planet. Sci. Lett.*, v. 458, p. 14–21.

431 Tucholke, B.E., Lin, J., and Kleinrock, M.C., 1998, Megamullions and mullion structure defining
432 oceanic metamorphic core complexes on the Mid-Atlantic Ridge: *J. Geophys. Res.*, v. 103, no.
433 B5, p. 9857–9866.

434 Xiao, H.-B., Dahlen, F.A., and Suppe, J., 1991, Mechanics of extensional wedges: *J. Geophys.*
435 *Res.*, v. 96, no. B6, p. 301–318.

436 Wilson, S.C., Murton, B.J., and Taylor, R.N., 2013, Mantle composition controls the development
437 of an Oceanic Core Complex: *Geochem. Geophys. Geosyst.*, v. 14., no. 4, doi:
438 10.1002/ggge.20046

439 Yuan, X.P., Leroy, Y.M., and Maillot, B., 2015, Tectonic and gravity extensional collapses in
440 overpressured cohesive and frictional wedges: *J. Geophys. Res.*, v. 120,
441 doi:10.1002/2014JB011612.

442

443 **Figure captions**

444

445 **Figure 1.** A–D: Seafloor terrain and slopes at four Mid-Atlantic Ridge detachment faults (locations
446 shown in inset E), from AUV bathymetric data gridded at 2 m resolution and plotted at equal scale.
447 Colored dots mark detachment termination, color-coded by $\mu_D (1 - \lambda_D)$ (see section 4). Red arrows
448 indicate spreading direction, pointing away from the ridge axis. Dashed lines show northernmost
449 and southernmost spreading-parallel profiles bracketing topographic profiles used here, which are
450 evenly spaced at 100 m. RR = rubble ridges, i.e., small fragments of broken-down apron carried
451 by the fault surface.

452

453 **Figure 2.** High-resolution bathymetric profiles oriented parallel to the transport direction (inferred
454 from corrugations), spaced 100 m apart between dashed lines in Fig. 1. Thin red/blue/black
455 sections are hanging wall / footwall / moat sections of each profile, respectively; thick gray lines
456 are linear fits used to obtain estimates for apron slope and detachment fault dip. A: TAG; B:
457 16°36'N OCC; C: South Core Complex; D: 13°20'N OCC.

458

459 **Figure 3.** A: Schematic cross section of the termination of the 13°20'N detachment fault, based on
460 topographic profile XX' from Fig. 1D. Inset shows a zoom on the hanging wall apron, with inferred
461 slip line orientations. Setup of corresponding critical taper model shown below. B: Stability
462 envelopes calculated using extensional taper model. These envelopes all account for slope of
463 13°20'N apron measured along crest profile, and all correspond to a specific range of $\mu_D (1 - \lambda_D)$
464 values = 0.15 ± 0.01 on the detachment fault.

465

466 **Figure 4.** Contours of best-fitting values of $\mu_D (1 - \lambda_D)$ on a detachment fault of dip β underlying an
467 apron of slope α , assuming a critical taper model with hydrostatic fluid pressure and an internal
468 friction angle of 30°. Symbols indicate measured slopes along the profiles bracketed in Fig. 1. hc:
469 hanging wall cutoff (termination).

470

471 **Figure 5.** Progressive rollover and exhumation of a detachment fault. Blue curve is rolling hinge
472 model of Buck (1988) for an elastic plate of flexural wavelength L (~ 1 km at the MAR, Schouten
473 et al., 2010). A: At moderate offsets (e.g., fault heave = $2L$), footwall slopes are steep, which leads

474 to mass wasting of the breakaway (fc: footwall cutoff) region, eventually forming the chaotic
475 terrain. B: At intermediate offsets (e.g., fault heave = $3L$) flexural rotation of the footwall leads to
476 very shallow seafloor slopes, promoting a widespread apron zone burying most of the detachment
477 surface. C: Finally, at large offsets (e.g., fault heave = $4L$) late-stage doming occurs close to the
478 fault termination (hc: hanging wall cutoff) where seafloor slopes increase, reducing the extent of
479 the apron and exposing the corrugated detachment surface (wiggly lines).

Figure 1

[Click here to download Figure: Figure_1_OCC_maps_SMALL.pdf](#)

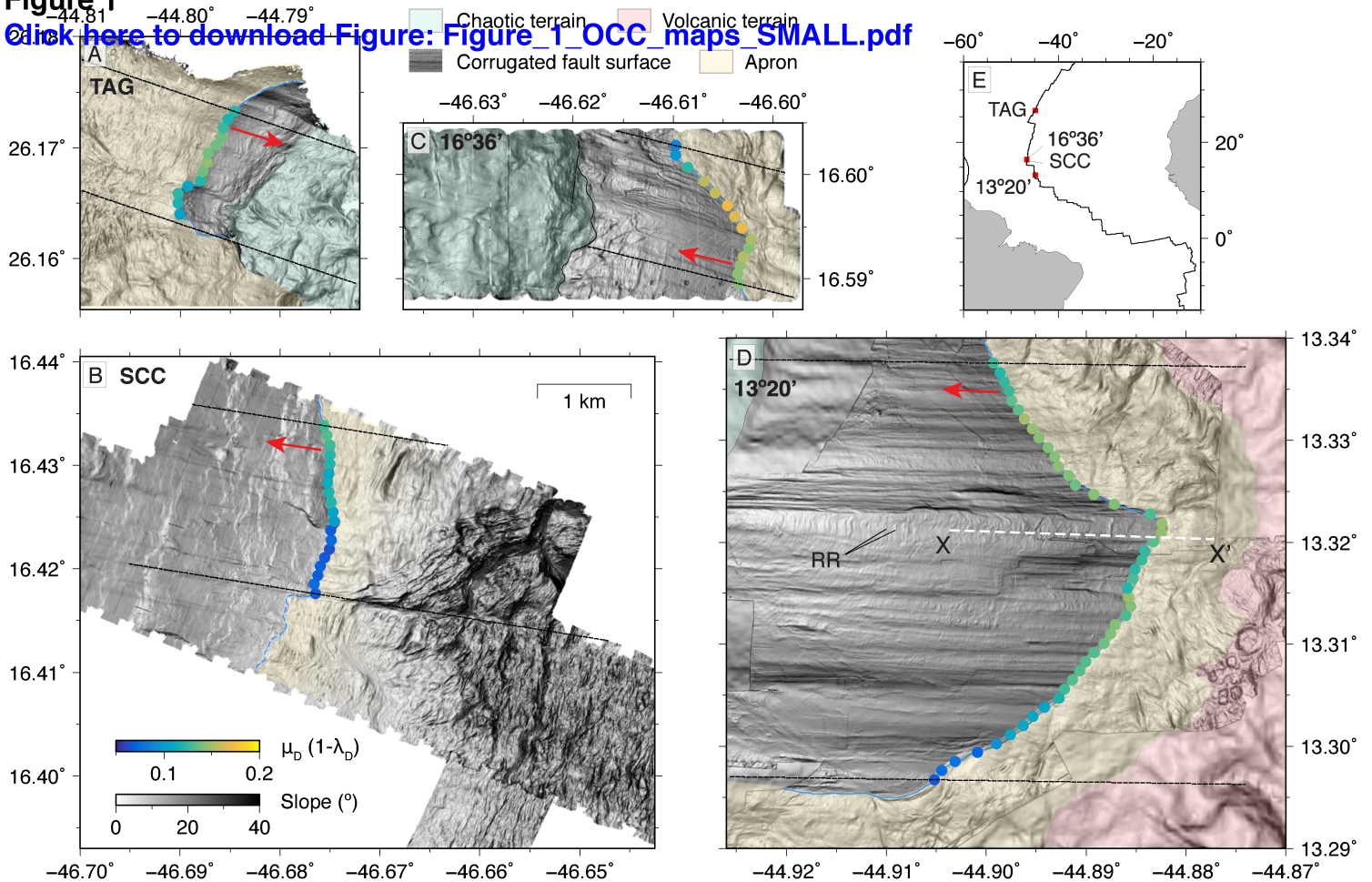


Figure 2

[Click here to download Figure: Figure_2_all_slopes.pdf](#)

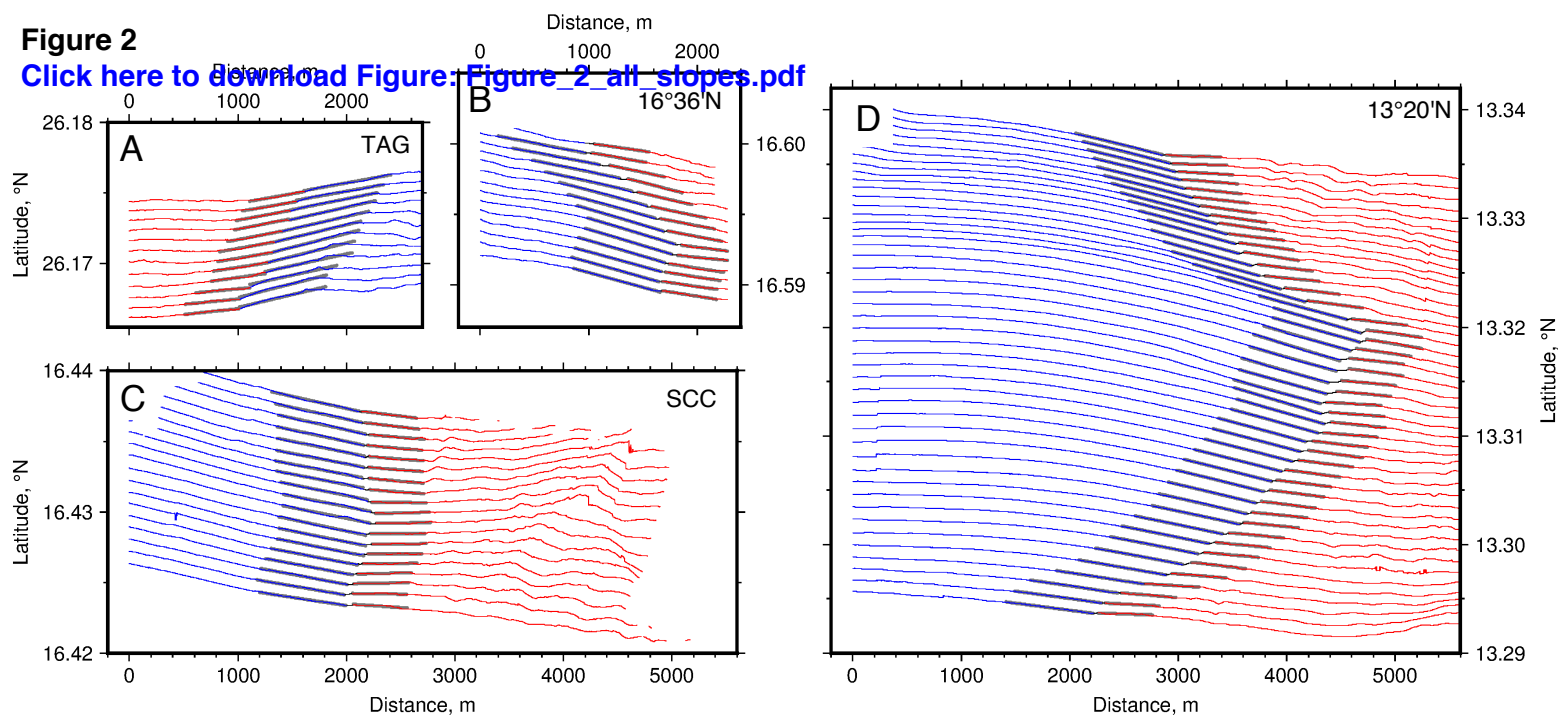
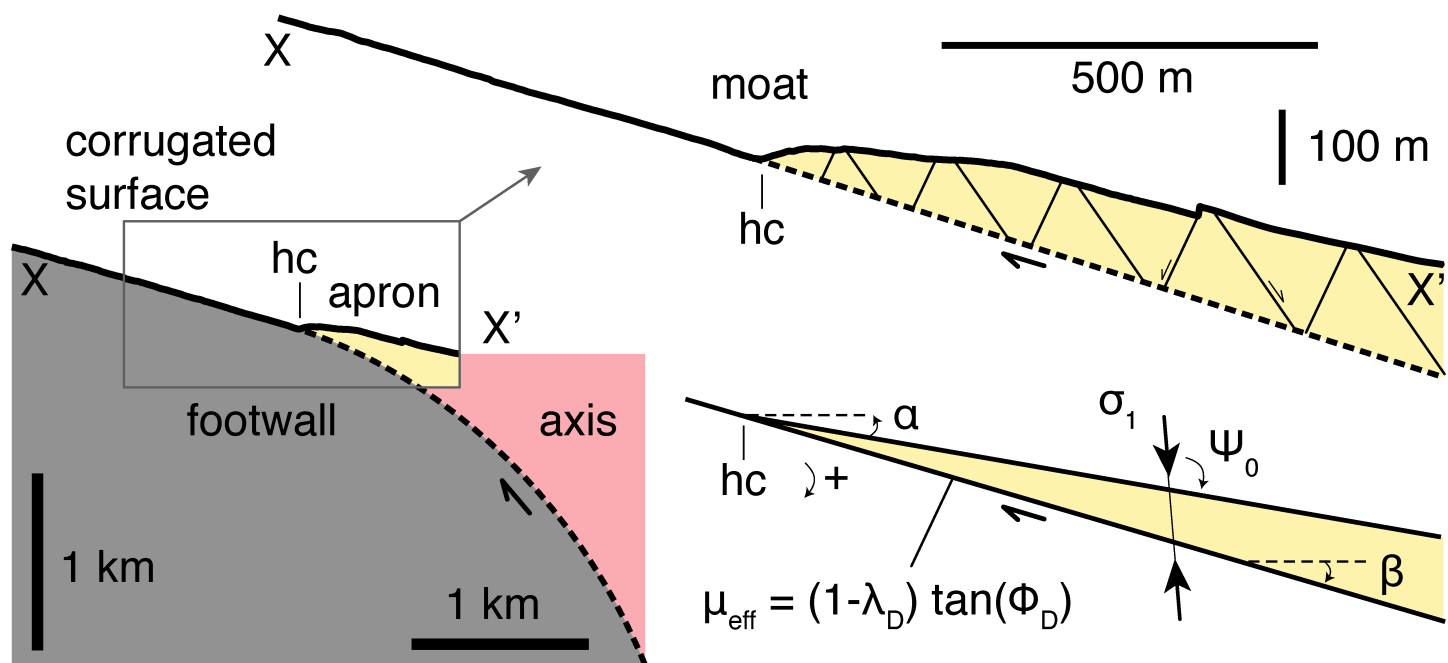


Figure 3

[Click here to download Figure: Figure_3_apron_model.pdf](#)

A



B

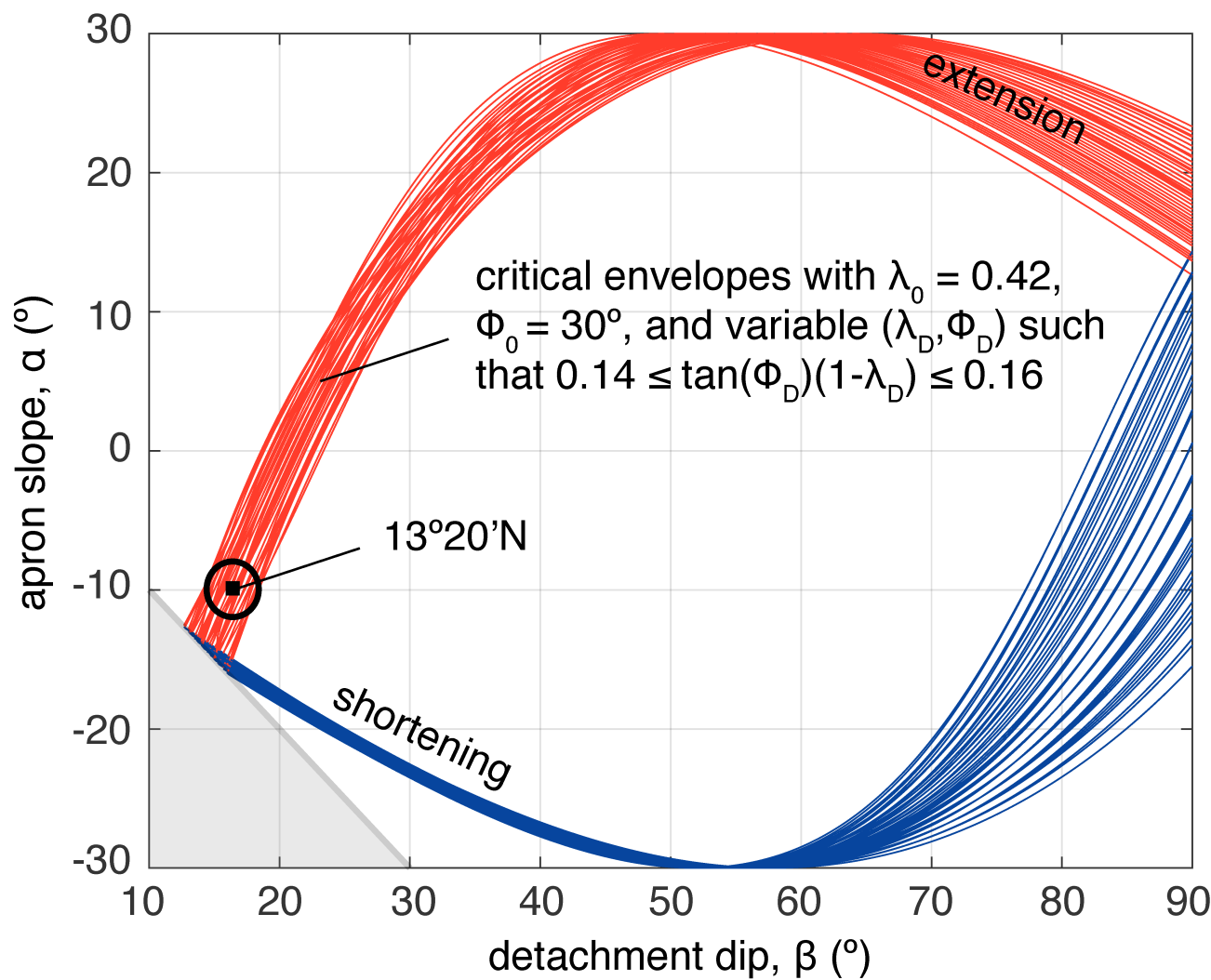


Figure 4

[Click here to download Figure: Figure_4_slopes2friction.pdf](#)

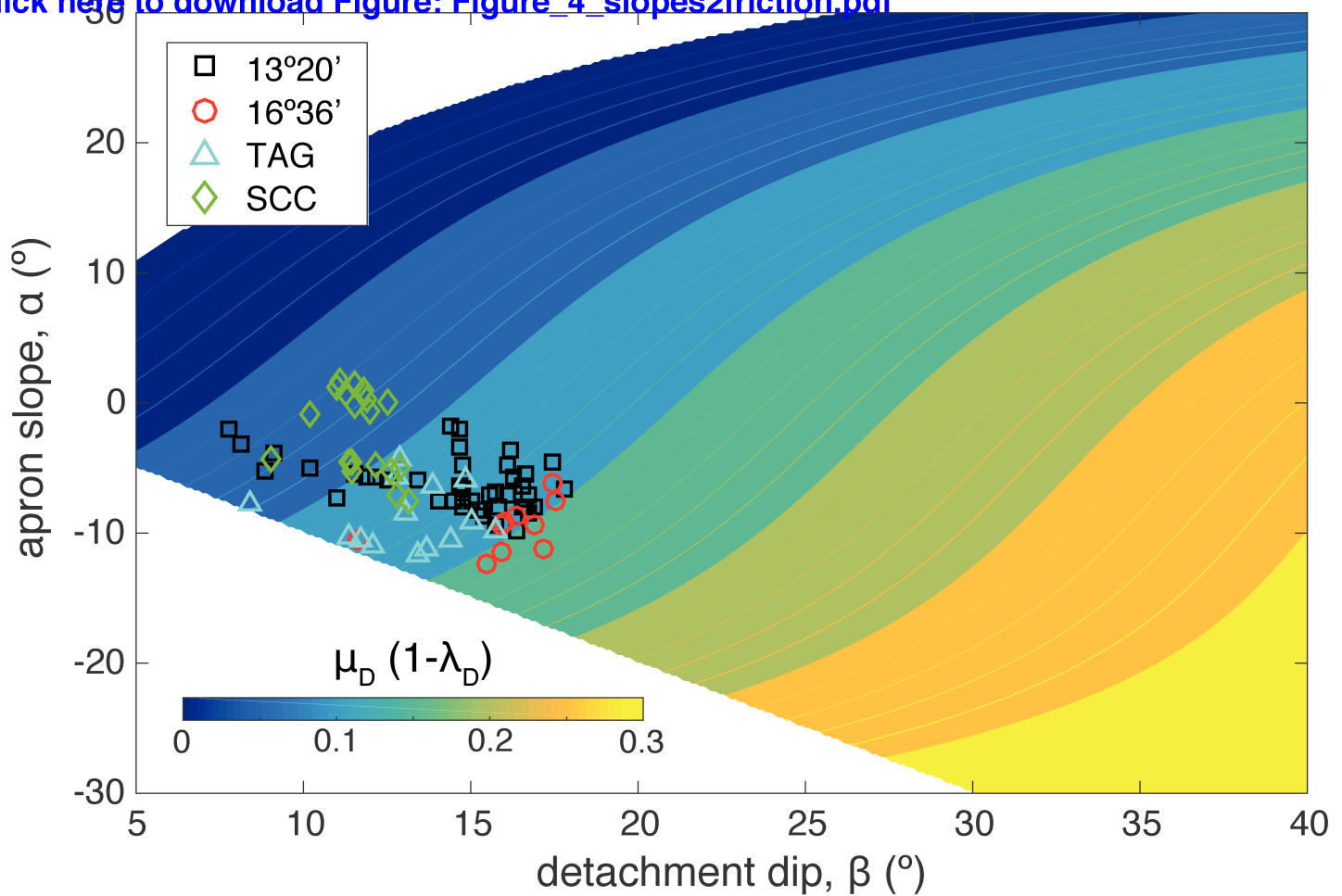


Figure 5

[Click here to download Figure: Figure_5_synthetic_cartoon.pdf](#)

